# Probing Co- and Fe-doped LaMO3 (M = Ga, Al) perovskites as thermal sensors

Olivier Toulemonde, Alexis Devoti, Patrick Rosa, Philippe Guionneau, Mathieu Duttine, Alain Wattiaux, Eric Lebraud, Nicolas Penin, Rodolphe Decourt, Alexandre Fargues, et al.

## To cite this version:

Olivier Toulemonde, Alexis Devoti, Patrick Rosa, Philippe Guionneau, Mathieu Duttine, et al.. Probing Co- and Fe-doped LaMO3 (M = Ga, Al) perovskites as thermal sensors. Dalton Transactions, 2018, 47 (2), pp.382-393. 10.1039/c7dt03647g . hal-01690082

# Probing Co- and Fe-doped $LaMO_3$ (M = Ga, Al) perovskites as thermal sensors, including spin-crossover evidences

Olivier Toulemonde, Alexis Devoti, Patrick Rosa, Philippe Guionneau, Mathieu Duttine, Alain Wattiaux, Eric Lebraud, Nicolas Penin, Rodolphe Decourt, Alexandre Fargues, Sonia Buffière, Alain Demourgues and Manuel Gaudon*

CNRS, Univ. Bordeaux, ICMCB, UPR 9048, F-33600 Pessac, France

*KEYWORDS. Spin Crossover, Perovskite, Thermochromism/ Thermochromic materials, Sensors.*

ABSTRACT: The synthesis of Co-doped or Fe-doped La(Ga,Al)$O_3$ perovskite from Pechini process aims at obtaining a color change induced by temperature and associated to Spin Crossover (SCO). In the Fe-doped samples, the iron is shown to be in the high spin state whereas a SCO from low spin to high spin configuration is detected on the Co-doped compounds when temperature increases. The Fe-doped compounds clearly adopt high spin configuration, even down to 4K, on the basis of Mossbauer spectroscopy analysis. The original SCO phenomenon on the Co-doped compounds $LaGa_{1-x}Co_xO_3$ $(0<x<0.1)$ is evidenced and discussed on the basis of *in situ* X-ray diffraction analysis and UV-vis spectroscopy. This SCO *versus* temperature is progressive and occurs in a broad range of temperature roughly between 300°C and 600°C. The determination of the crystal field about 2 eV and the Racah parameter B around 500 $cm^{-1}$ for $Co^{3+}$ ($3d^6$) ions show that these values allow the SCO occurrence. Hence, this study shows the possibility to use $LaGa_{1-x}Co_xO_3$ compounds as thermal sensor for low Co content (x=0.02). The competition between steric and electronic effects in $LaGaO_3$ where $Co^{3+}$ is stabilized in the LS state, shows that electronic effects with the creation of M-O covalent bonds are predominant and contribute to stabilize a high crystal field around $Co^{3+}$ (LS) despite its smaller ionic radius compared to the one of $Ga^{3+}$.

**Introduction.** Since a few decades, the X-chromic inorganic oxides and the Spin Crossover (SCO) molecular materials scientific communities have successfully ran in parallel towards sensing applications. The SCO phenomenon corresponds to a stimulus-induced modification of the electronic configuration in ($d^4$–$d^7$) transition metals leading to a switch of optical, magnetic and mechanical (structural) properties (Fig.1, top side). It has been intensively studied for more than three decades by the international research community for the fundamental richness it offers with a view to promising potential applications in the fields of information storage, smart pigments and captors.[1-7] The main part of research efforts have been concentrated on molecular complexes based materials and coordination polymers so far.[1-4, 8-15] The diversity of molecular complexes and coordination polymers combined to the multiple possibilities to induce SCO - *a modification of temperature, pressure, chemical environment or the use of light* - has allowed getting a large panel of SCO materials with an extreme diversity of switch behaviors, going from large hysteretic transitions to smooth conversion. Such diversity has given access to a fine fundamental understanding of the SCO phenomenon, even though many aspects are still debated, and has been used to feed diverse pioneering research fields such as nanoparticles design,[16-22] or photo-crystallography for instance.[23-24] In particular, the crucial but intricate role of the structural-properties relationship in SCO solids has been evidenced.[25-29] From the X-chromic point of view, let us already note that one weak point of molecular based SCO materials is the relatively small panel of colors available so far.

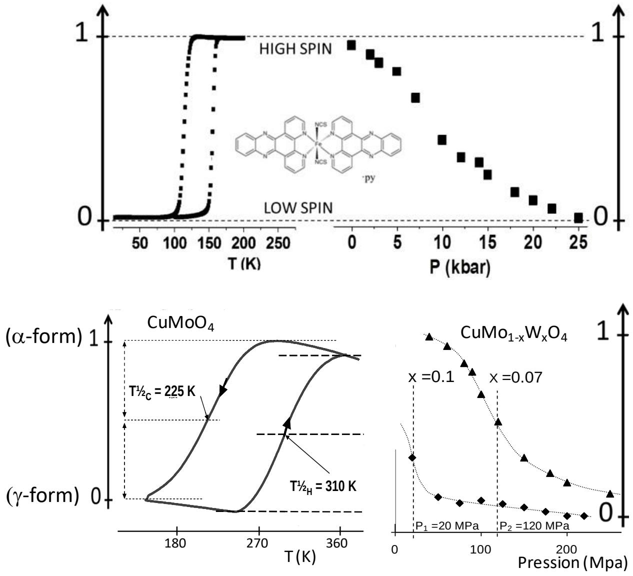

Figure 1: *Top side*- Thermo-switch in a molecular complex showing a progressive transition with a large hysteresis centered on room temperature and piezo-switch showing a very smooth conversion.[7] *Bottom side*- Example of the thermo- and piezo-induced phase transition between α- and γ-phases for $CuMo_{1-x}W_xO_4$ oxides (bottom side).[51]

Then, two classes of X-chromic materials based on oxide are studied in parallel. The first one is based on a chemical reaction associated with a redox reaction (for illustration see the $V_2O_5$ oxide for electrochromism,[30-36] or $WO_3$ oxide for electrochromic,[37-40] or photochromic,[41-44] properties for the smart windows concept). The second class of material for which the change of optical properties is associated with a phase transition allowing piezo- & thermo-chromic properties (see Fig. 1, bottom side). This field associated with a phase transition is of growing interest. There are numerous recent works dealing with thermochromic properties of vanadium oxide thin films linked to monoclinic-rutile structural transition.[45-47] To date, mainly developed in our institute in the past decade, X-chromic properties of $AMoO_4$ compounds were explored with the aim to tune the thermochromic phase transition temperature or the piezochromic phase transition pressure of these molybdates via the composition - *through the control of the ionic-covalent character of the chemical bonding*,[48-49] or via their crystallite sizes.[50] A large pallet of desirable properties for various requirements is now accessible thanks to this past research. Especially, oxide materials offer a large panel of colors.

Considering the two X-chromic material families stated above, mixing the SCO and inorganic oxides fields can offer a good opportunity to get a synergy between their specific properties. In particular, it is proposed for the first time to explore X-chromic effects associated to SCO in oxides that should allow overcoming the poor cyclability shown by X-chromic oxides and the inadequate low working temperatures shown by molecular complexes.

Pressure or temperature induced SCO oxides are already known. However, the main examples available on pressure induced SCO oxides are admittedly dealing with reversible transition but at very high pressure in the GPa range,[52,53] limiting drastically the industrial interest of the observation. Regarding the temperature-induced SCO in oxides, it seems nearly limited to some cobalt oxides, and especially on $RECoO_3$ perovskite-type structure (RE = Rare Earth metal)[54] where the transition metal is located in a relatively intense octahedral field with a 10Dq/B ratio corresponding to the Low Spin state (LS) evolving *versus* temperature to Intermediate (IS),[55-57] or High Spin (HS)[58-60]. The reported temperature transition occurs over a broad range from 200K for $LaCoO_3$ up to 800K for $YCoO_3$ respectively.[54] Interestingly, this range of temperature appears already much wider than the one known for molecular SCO materials but oxides are unfortunately black-colored and so without any interesting chromatic properties. Regarding the $Co^{3+}$ diluted approaches, one can pointed out $LaCo_{1-x}Al_xO_3$ solid solution studies which proposed to tune the SCO temperature up to 245K in $LaCo_{0.5}Al_{0.5}O_3$.[61] And when diamagnetic matrices were considered as for example in $LaCo_{0.02}Al_{0.98}Co_{0.02}O_3$ and $LaNi_{0.01}Al_{0.99}O_3$ oxides, the thermo-chromic effects have not been studied yet since the magnetic and optical characterizations were only carried out up to room temperature.[62]

That is why we explore the thermochromic properties of Fe-doped and Co-doped $La(Al/Ga)O_3$ diamagnetic matrix derived from the cubic perovskite structure aiming to propose a new generation of SCO oxides. Indeed, the original compounds obtained with low cobalt or iron concentration in $LaGaO_3$ matrices can open new windows for thermochromic phenomena, as useful as *in situ* thermal sensors for illustration. No observation of an eventual $Fe^{3+}$ spin crossover in similar perovskite has been reported so far contrary to $Co^{3+}$ that might be in relation with thermochromic properties. In this paper, Fe-doped and Co-doped $La(Al/Ga)O_3$ are synthesized using a Pechini route. To study their ability to be used as thermal sensors thanks to a SCO phenomenon, the spin state of the paramagnetic ions is studied *versus* temperature using *in situ* optical spectroscopy and X-ray diffraction.

**Experimental.** The Fe-doped and Co-doped $La(Al/Ga)O_3$ compounds were synthesized using the Pechini route.[63] This chemical process is based on cations chelation by citric acid (CA) and on polyesterification between CA and ethylene glycol (EG) which leads to the formation of a polycationic resin. Aqueous solutions of citrate were prepared by dissolving CA in a minimal volume of water. Then, cationic salts: $La(NO_3)_3\,6H_2O$, $Fe(NO_3)_3\,6H_2O$ or $Co(NO_3)_2\,6H_2O$, $Ga(NO_3)_3\,xH_2O$ (with x calculated to 4.0 by thermogravimetric titration), were added after dissolution in a minimum of water to the citric acid solution. A CA/cations molar ratio equal to 3/1 was used. After complete dissolution of the metallic salts, EG was added with a 4/1 EG/CA molar ratio. EG-CA polymerization was promoted by removing water with continuous heating on a hot plate. Then, a two-step thermal treatment was apply to the highly viscous mixtures: first, a calcination at 400°C for 10 h and then, an annealing dwell for 20h at the final temperature of 800°C. For the annealing step the heating and cooling rates are fixed at 4°C/min.

Powder X-Ray Diffraction (PXRD) measurements were carried out on a PANalytical X'PERT PRO diffractometer equipped with an X-celerator detector, using Cu-$K\alpha_1$ radiation. The unit cell parameters were refined by structural pattern matching using the Fullprof® program package. All the patterns were analyzed using the Caglioti function, *i.e.* the isotropic peak profile function for which the u, v, w and shape parameters are refined. For the *in situ* high temperature characterizations, the experiments were made on a PANalytical X'pert, with Bragg-Bentano, geometry, equipped with a back monochromator ($K\alpha$ =1,5418 Å and an Anton-Paar HTK16 chamber. The chosen heating thermal sequence has allowed the recording of the $LaGa_{0.9}Co_{0.1}O_3$ diffractograms (Space group: *R*-3*c*) between room temperature and 800°C.

Mössbauer spectra were recorded in transmission geometry using a constant acceleration Halder–type spectrometer with a room temperature $^{57}Co$ source (Rh matrix). The velocity scale was calibrated using a pure metal iron foil. The polycrystalline absorbers containing about 10 mg/cm$^2$ of iron were placed into a cryostat (liquid He) in order to collect $^{57}Fe$ Mössbauer spectra at 4.2 K. Refinement of the Mössbauer hyperfine parameters ($\delta$ isomer shift, $\Delta$ quadrupole splitting, $\varepsilon$ quadrupole shift, H hyperfine field, $\Gamma$ signal linewidth and relative areas) was performed using homemade programs and the WinNormos® software.

Diffuse absorption spectra were recorded at room temperature from 200 to 800 nm on a Cary 17 spectrophotometer using an integration sphere (spectral resolution: 1 nm and band length: 2 nm). Halon was used as white reference. RGB space colorimetric parameters were determined from the spectra using a two-step mathematic treatment. The first step consists in extracting the XYZ tri-stimulus values (defined by the CIE, 1964) from the integration (over the visible range, *i.e.* from $\lambda$ = 380 nm up to 780 nm) of the product of $x(\lambda)$, $y(\lambda)$ or $z(\lambda)$ functions (CIE – 1964) with the diffuse reflectance spectra function $X = \int x(\lambda).R(\lambda)d\,\lambda$. Then, we used the transfer equations defined by the CIE, 1976, to transform the XYZ space to the L*, a* and b* common three-color space parameters. The *in situ* measurement *versus* temperature are obtained using visible spectra in the 400 - 800 nm range between room temperature and 600°C recorded on a setup equipped with a photomultiplicator linked to a multichannel fiber. The sample is heated and cooled thanks to a Linkam TS1000 (room T°-1000°C) cell device. A first fiber directs a white light source on the sample; a second fiber transmits the diffuse reflectivity of the sample to a BWTek (BTC112E) spectrophotometer. The reflectivity of the sample ($R_S$%) was estimated using a white reference ($BaCO_3$ with RW% of reflectivity) and a black one ($Mn_2O_3$ with $R_B$% of reflectivity) from the equation: $R_S\% = (R_S\%-R_B\%)/(R_W\%-R_B\%)$.

In order to determine magnetic properties of these compounds, measurements at low temperature were made with a superconducting quantum interference device Quantum Design MPMS-7XL magnetometer from 2 K to 300 K at applied fields of up to ±5 T. The measurements presented here were performed typically at 2 K. A large amount of powder (typically 200 mg) was introduced into a capsule to obtain immobilized and randomly oriented powder particles for the measurements. The diamagnetic contributions from the core electrons and from the sample holder were subtracted to the raw signal.

## **Results and discussion**.

### - Fe-doped La(Al/Ga)$O_3$ compounds

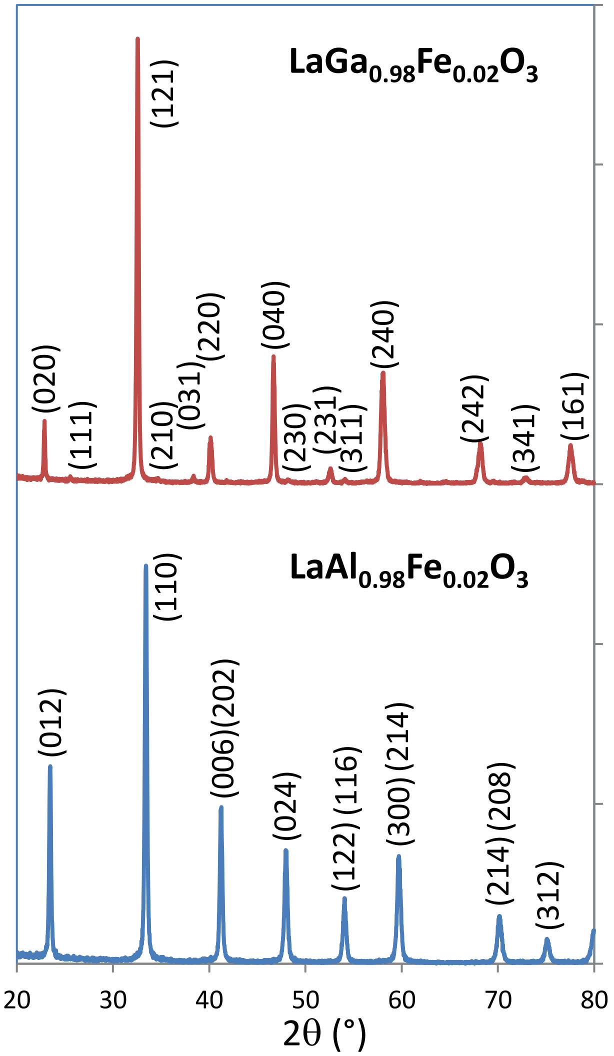

Figure 2: X-ray diffraction patterns of 0.02 mol% Fe-doped aluminate and gallate compounds. The gallate compound with orthorhombic distortion is indexed from JCPDS 00-024-1102 and the aluminate compound with rhombohedral distortion is indexed from JCPDS 00-048-0123.

The first part is devoted to the Fe-doped La(Al/Ga)$O_3$ compounds. Herein, the results obtained on the 2 mol% Fe-doped $LaGaO_3$ and $LaAlO_3$ are especially selected and commented for comparison. Indeed, the results obtained on 5 and 10 mol%-doped compounds did not evidence any change of behavior *versus* the doping concentration. X-ray diffraction patterns of the 2 mol% Fe-doped $LaGaO_3$ and Fe-doped $LaAlO_3$ compounds are reported in Figure 2. The two compounds crystallize into a pure perovskite phase with a submicronic crystallinity. An average isotropic crystallite size of about 50 nm can be extracted using Scherrer law from the X-ray peak widths, with $LaB_6$ used to calibrate the apparatus enlargement. The gallate phase crystallizes into the *Pbmn* orthorhombic space group whereas the aluminate phase crystallizes into the *R*-3*c* trigonal space group. The orthorhombic and rhombohedral distortions observed for the $LaGaO_3$ and the $LaAlO_3$ matrix compositions, respectively are in good agreement with the tolerance factor *t* value: $t = (r_{La} + r_O)/[\sqrt{2}\times(r_{Ga/Al}+r_O)]$ - with $r_O$, $r_{Ga}$, $r_{Al}$ and $r_{La}$ ionic radius of $O^{2-}$, $Ga^3$+, $Al^{3+}$ and $La^{3+}$ ions, respectively, leading to $t = 0.96$ for $LaGaO_3$ and *t* near 1 for $LaAlO_3$ - and the literature.[64,65]

Absorption spectra of the two $LaM_{0.98}Fe_{0.02}O_3$ compounds (with M = Al or Ga) compounds are reported in Figure 3. From the Tanabe-Sugano diagram of $d^5$ electronic configuration metal, the High-Spin state (HS state) does not exhibit allowed electronic transitions in octahedral field. Indeed, in the HS state all the electronic transitions from the fundamental level state are associated with a spin flipping ($\Delta S \neq 0$). On the contrary, 4 authorized electronic transitions are expected for the Low-Spin state configuration (LS state): $^2T_1 \leftarrow {}^2T_2$; $^2A_2 \leftarrow {}^2T_2$, $^2E \leftarrow {}^2T_2$, $^2A_1 \leftarrow {}^2T_2$. The two absorption spectra are predominantly marked by high energy charge transfers (CTB) with an onset which can be located at about 625 and 500 nm, for aluminate and gallate compounds, respectively. The CTB onset being in the visible range, it produces a pale yellowish coloration for the two compounds together with a more saturated yellow color for the aluminate than for the gallate. Taking into account the Pauling electronegativity, the ionic radii of various ions ($Ga^{3+}$: $r_{ionic} = 0.62$ Å and $X_{Pauling} = 1.81$ compared to $Al^{3+}$: $r_{ionic} = 0.535$ Å and $X_{Pauling} = 1.61$) and the stabilization of $Fe^{3+}$ species in octahedral site, the $O^{2-} \rightarrow Ga^{3+}$ CTB is expected at lower energy than the $O^{2-} \rightarrow Al^{3+}$ CTB (α-$Ga_2O_3$, $E_g$=4.4 eV, α-$Al_2O_3$, $E_g$=8.7 eV for instance). Then, the CTB observed on Figure 3 can be attributed to the $O^{2-} \rightarrow Fe^{3+}$ charge transfer involving 2p(O) band and $t_{2g}$(Fe) level. The higher stabilization of $t_{2g}$ levels of $Fe^{3+}$ in $LaAlO_3$ because of lower Fe-O bond distances than in $LaGaO_3$ contribute towards an $O^{2-} \rightarrow Fe^{3+}$ CTB at lower energy in $LaAlO_3$ compared to that in $LaGaO_3$. Moreover, the absence on the whole 200 nm - 1500 nm range of quite intense d-d bands suggests a High-Spin state situation for the $Fe^{3+}$ ions in both compounds at room temperature as it will be confirmed later on thanks to Mossbauer spectroscopy study.

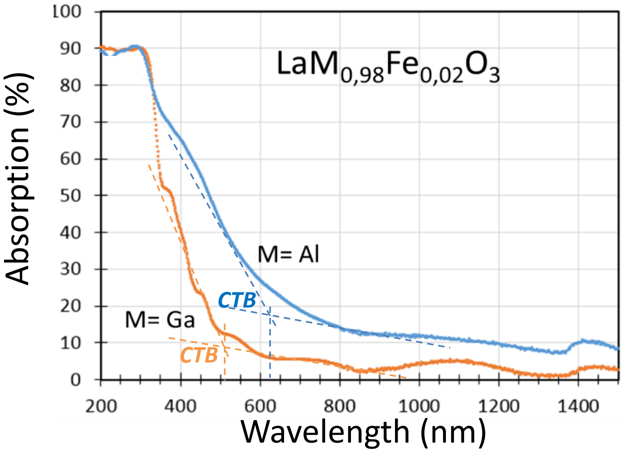

Figure 3: UV-vis-NIR Absorption spectra, obtained after transformation of the diffuse reflectance spectra considering the absorption percentage such as: $A\% = 100 - R_{diff.}\%$, of the Fe-doped La(Al/Ga)$O_3$ compounds.

Magnetization loops *versus* applied field/temperature ratio recorded at 2.0 K on Fe-doped La(Al/Ga)$O_3$ compounds are superimposed for clear comparison in Figure 4. It can be clearly seen that the matrix composition does not influence the magnetization properties which are obtained. Both signals are mainly paramagnetic. The data treatment and the following discussion is then limited to $LaGa_{0.98}Fe_{0.02}O_3$ compound. The data were fitted (Figure 5) considering a Langevin paramagnetic behavior following the equation:

$$< M >= n\mu_{ef}\left[\coth\left(\frac{\mu_{eff}H}{k_BT}\right)-\frac{k_BT}{\mu_{eff}H}\right],$$

with <M> the experimental magnetization, $\mu_{eff}$ the effective magnetic moment of paramagnetic species, *H/T* the applied field : temperature ratio, $k_B$ the Boltzmann constant and *n* the molar concentration of paramagnetic cations per mol. Two fits were attempted: - the first one with $\mu_{eff}$ as the only parameter to refine considering *n* paramagnetic ions concentration equal to the theoretical one: 0.02; - the second one with *n* paramagnetic ions concentration and $\mu_{eff}$ parameters allowed to refine starting with $\mu_{eff}$ equal to the theoretical 5.92 μB value for $Fe^{3+}$ ions in HS state

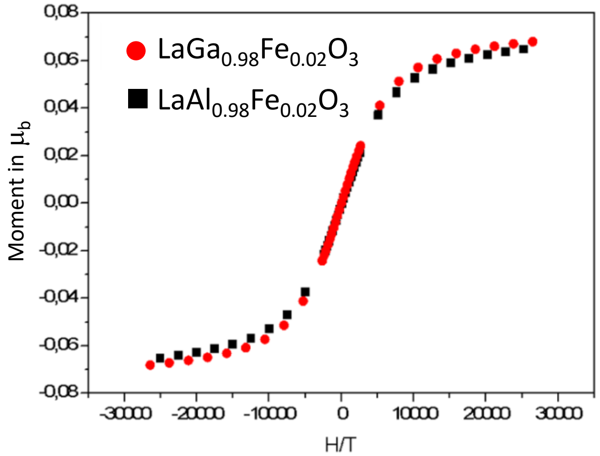

Figure 4: Magnetization curves: magnetic moment (in μB) *versus* H/T (Oe.$K^{-1}$) collected at T=2K for Fe-doped $LaGaO_3$ and $LaAlO_3$ compounds.

The two fits correctly match the experimental curve, with obviously a better correlation factor for the second model. For the first fit, the $\mu_{eff}$ that can be extracted is found equal to 4.2 μB; for the second fit, the paramagnetic concentration *n* that is extracted is equal to 0.0133 with an extracted $\mu_{eff}$ equal to 5.72 μB. The discrepancy between the total number of paramagnetic ions suggested by this second fit and the targeted 2 mol% Fe is in the order of 33%. Interestingly such discrepancy is on the same range of magnitude when the data obtained for $LaAl_{0.98}Fe_{0.02}O_3$ compound are fitted. It is quite high to be only due to stoichiometric problem. That is why, in Figure 6 is reported the evolution of the effective moment extracted from fits using the first model, *i.e.* fixing the paramagnetic ions concentration n to 0.02, from various magnetization curves recorded between 2K and 300K even with the slight discrepancy with respect to the experimental curve. It is important to note that it is possible to plot the evolution of the *n* paramagnetic ions concentration from a similar procedure but using the second model. Indeed both approaches lead to the same tendency of the n parameter and/or the $\mu_{eff}$ effective paramagnetic moment *versus* temperature. Thus it can be said that, at high temperature, the awaited paramagnetic magnetization is not fully reached: some missing paramagnetic ions and/or a lower effective moment than the theoretical one for the $Fe^{3+}$ ions can both explain the phenomenon. Further, at low temperature, the deviation between the extracted $\mu_{eff}$ effective paramagnetic moment and the theoretical one is all the more important as the temperature decreases, with a “threshold” temperature about 60K. Different explanations can be put forward: (i) the effective moment is lower than the theoretical one due to zero field splitting phenomenon, the effect on the effective moment becoming quite significant for temperatures below 60 K; (ii) the effective moment is lower than the theoretical one due to a High-Spin/Low-Spin states mixture, the discontinuity of the $\mu_{eff}$ *vs* T ° curve can then be interpreted as a SCO transition ; (iii) the effective moment is the theoretical one, the missing magnetization comes from antiferromagnetic interactions between iron species as already pointed out in Co doped ZnO matrix,[66-67] the strength of these antiferromagnetic interactions increasing in a standard manner with decreasing temperature.

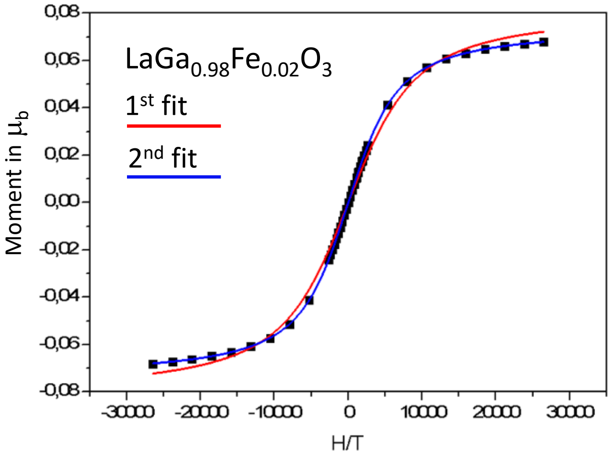

Figure 5: Magnetization curve: magnetic moment (in μB) *versus* H/T (Oe.$K^{-1}$) collected at T=2K for Fe-doped $LaGaO_3$ and the two calculated curves issued from the two tested fit models. See text for definition of the fits.

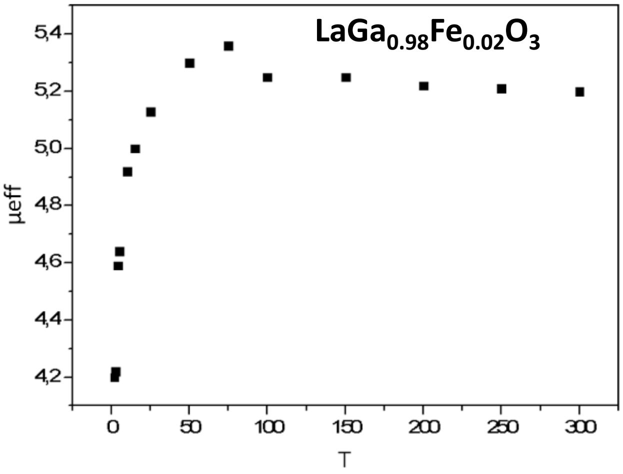

Figure 6: effective moment in μB unit $LaGaO_3$ deduced from the magnetization curves recorded between 2 and 300K using the first fit approach.

Having in mind that the present study aims to correlate thermochromic properties with SCO transition, $^{57}Fe$ Mössbauer spectroscopy (Figure 7) was performed to test the possible occurrence of SCO.

At room temperature, the $^{57}Fe$ Mössbauer spectrum of $LaGa_{0.98}(^{57}Fe)_{0.02}O_3$ can be reconstructed with a sum of quadrupole doublets with Lorentzian shape (linewidth: 0.30 mm/s), with the same isomer shift but different quadrupole splitting values (*ie.* with a “distribution of quadrupole splitting values”). The hyperfine parameters reported in Table 1, isomer shift (about 0.37 mm/s) and quadrupole splitting (<Δ> = 0.70 mm/s), are characteristic of high-spin trivalent iron ions in octahedral environment. Considering that $Fe^{3+}$ is in a high-spin state and that the 6S ground state has a spherically symmetric distribution of electronic charge, the quadrupole splitting arises mainly from the lattice contribution to the electric field gradient (EFG) through the crystal field produced by ligands and first-neighbor cations at the $^{57}$Fe nucleus. Then, the observed distribution of quadrupole splitting clearly reflects slight variations of the EFG due to some local disorder or heterogeneity in site distortion. At 4.2 K, the spectrum is slightly shifted towards high energies (high velocity) due to the second-order Doppler effect but more interestingly in the context of our study, neither magnetically ordered component nor SCO phenomenon was actually evidenced for this material.

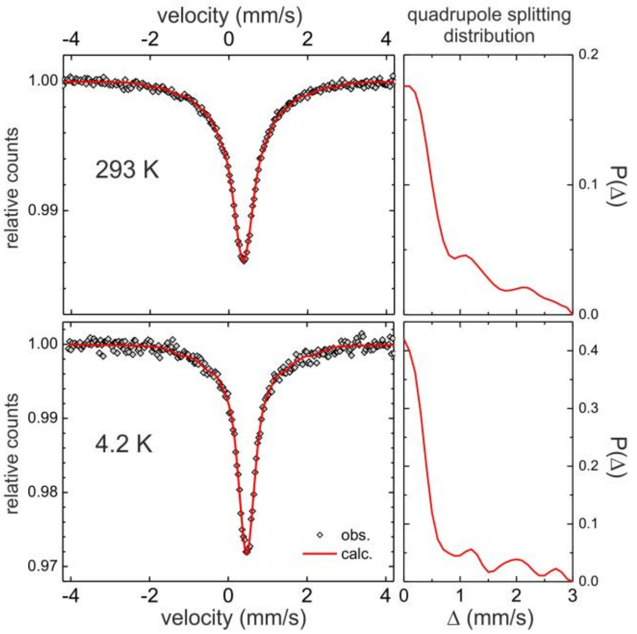

Figure 7: $^{57}$Fe Mössbauer spectra of $LaGa_{0.98}(^{57}Fe)_{0.02}O_3$ recorded at room temperature (293 K) and 4.2 K. Both spectra were calculated using a distribution of quadrupole splitting (Δ).

TABLE 1. $^{57}$Fe Mössbauer parameters determined from the fitting of $LaGa_{0.98}(^{57}Fe)_{0.02}O_3$ spectra recorded at room temperature and at 4.2 K.

| T | δ (mm/s) | <Δ>* (mm/s) | Γ (mm/s) |
|---|---|---|---|
| 293 K | 0.369(2) | 0.70 | 0.30 |
| 4.2 K | 0.465(2) | 0.57 | 0.30 |

*mean value of quadrupole splitting distribution.

### - Co-doped $LaGaO_3$ compounds

The second part is devoted to the Co-doped $LaGaO_3$ compounds with various $Co^{3+}$ ion concentrations between 0 and 50mol%. X-ray diffraction patterns of the various prepared compounds are reported in Figure 8. The Co-doped compounds crystallize into a pure perovskite phase, with an orthorhombic distortion observed for low cobalt concentrations ($x \leq 0.05$) whereas a rhombohedral distortion is identified for high cobalt concentrations ($x \geq 0.1$). The decrease of the unit-cell distortion from orthorhombic to rhombohedral network is in good agreement with a tolerance factor becoming closer and closer to the unit value ($t$ =1) as the larger $Ga^{3+}$ ions are replaced by smaller $Co^{3+}$ ions. As illustration, from the Shannon ionic radii of 1.36 Å ($La^{3+}$), 0.62 Å ($Ga^{3+}$), 0.61 Å (HS-$Co^{3+}$), 0.525 Å (LS-$Co^{3+}$) and 1.40 Å ($O^{2-}$), the $t$ factor for $LaGaO_3$ is calculated to be equal to 0.952 against 0.957 for $LaCoO_3$ considering $Co^{3+}$ in HS state. One should notice that the ionic size of HS-$Co^{3+}$ is close to that of $Ga^{3+}$ whereas the ionic radius of LS-$Co^{3+}$ is close to that of $Al^{3+}$ (0.535 Å).

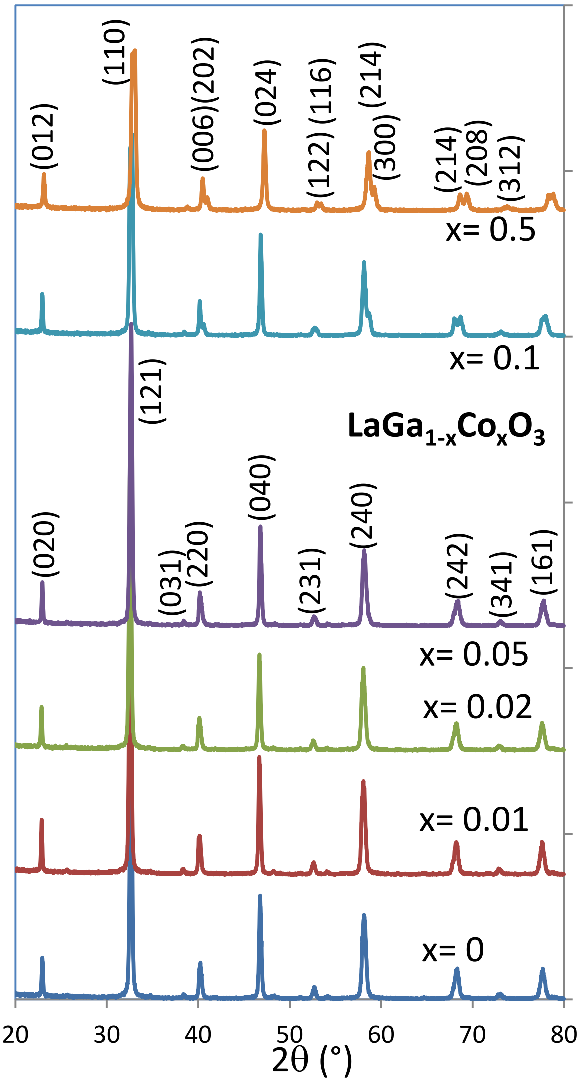

Figure 8: Powder X-ray diffraction patterns of xmol% Co-doped gallate compounds. Orthorhombic distortion is indexed from JCPDS 00-024-1102 and rhombohedral distortion is indexed from JCPDS 00-048-0123.

Absorption spectra of the Co-doped $LaGa_{1-x}Co_xO_3$ compounds with $0 \leq x \leq 0.1$ are reported in Figure 9. Besides the high energy Charge Transfer Bands around 4.4eV corresponding to $O^{2-} \rightarrow Ga^{3+}$ in $LaGaO_3$ and around 2.7 eV for $O^{2-} \rightarrow Co^{3+}$ in $LaGa_{0.99}Co_{0.01}O_3$, the important information is the occurrence of two absorption bands at lower energies with their intensity drastically increasing *versus* the cobalt concentration. These absorption phenomena can be attributed without any ambiguities to intra-atomic d-d transitions involving $Co^{3+}$ ions. From the Tanabe-Sugano diagram related to $d^6$ electronic configuration, the two visible absorption bands in the visible region about 450-500 nm and 750-780 nm can be indexed considering the $Co^{3+}$ chromophore in the LS state with the following $^1T_2 \leftarrow ^1A_1$, $^1T_1 \leftarrow ^1A_1$ transitions respectively. As we mentioned previously, the ionic radius of $Co^{3+}$ in the HS state is close to the one of $Ga^{3+}$ and stabilization of $Co^{3+}$ in the LS state in these compounds was not expected. Furthermore, the $Co^{3+}$ ion adopts at room temperature the HS state in $LaCoO_3$. For the $d^6$ electronic configuration corresponding to low crystal field (HS), only one intense $^5E \leftarrow ^5T_2$ transition, usually occurring around 600 nm, is expected. So the occurrence of $Co^{3+}$ stabilized in the LS state in $LaGa_{1-x}Co_xO_3$ for low Co concentrations is shown unambiguously. These two bands produce a brownish coloration whatever the low Co rate, with a darker color as the cobalt concentration increases. For the 10mol% cobalt concentration, the compound color is almost black as expected from Figure 9 and the symmetry of the crystal structure turns to trigonal. It has to be noted, additionally, that the linear increase of the absorption bands versus cobalt concentration (see Fig. S2) is a clear indication for the incorporation of the whole cobalt concentration inside the perovskite network.

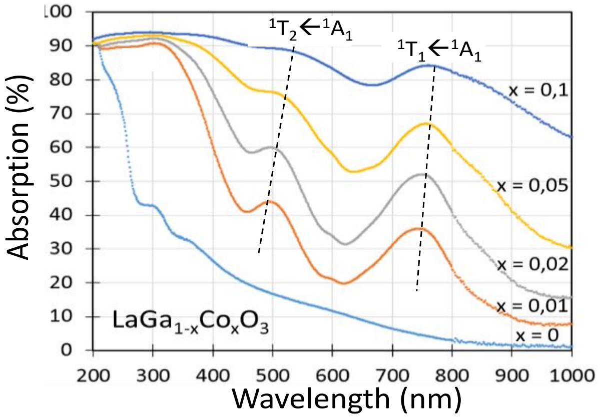

Figure 9: UV-vis-NIR Absorption spectra obtained after transformation of the diffuse reflectance spectra considering the absorption percentage such as: $A\% = 100 - R_{diff.}\%$, of the Co-doped $LaGa_{1-x}Co_xO3$ compounds with $0 \leq x \leq 0.1$.

Hence, only low cobalt concentrations with orthorhombic distortion allow colors away from grey level (moderate L* parameter) in order to study thermochromics applications related to the SCO effect when temperature increases. Furthermore, it can also be seen that the two absorption bands are red shifted when the cobalt concentration increases, particularly so for the $^1T_2 \leftarrow ^1A_1$ transition at higher energy. These two absorption bands being associated to an intra-atomic electron transfer from $t_{2g}$ to $e_g$ atomic orbitals, the red shift observed could mean in first approximation that the crystal field intensity slightly decreases while the $Ga^{3+}$ ions are substituted for $Co^{3+}$ ones. This is a paradox if we consider that the cobalt (III) ionic radius in the LS state in significantly lower than the $Ga^{3+}$ one. A careful spectroscopic calculation from the Tanabe-Sugano diagram for the $d^6$ electronic configuration yields a Racah parameter B varying from about 550 $cm^{-1}$ to 500 $cm^{-1}$ and a crystal field varying from 1.93 eV up to 2.01 eV for cobalt contents equal to 1% and 10%, respectively (see Figure S1). The red-shift observed is thus due to a decrease of the Racah parameter B *versus* the increase of cobalt content (increase of the covalence and decrease of the intra-atomic Coulomb repulsion), but is associated to a slight increase of the crystal field. Thus, in $LaGaO_3$ matrix, the lowest the cobalt concentration, the more unstable the LS state is in comparison to the HS state.

The magnetization *versus* applied field/temperature ratio at 5K for the 5 mol% Co-doped $LaGaO_3$ compound is superimposed to the magnetization signal of the 5 mol% Fe-doped $LaGaO_3$ compound, for comparison (Figure 10). The magnetization curves clearly show that cobalt ions are mostly diamagnetic, even if it shows a small paramagnetic residue.

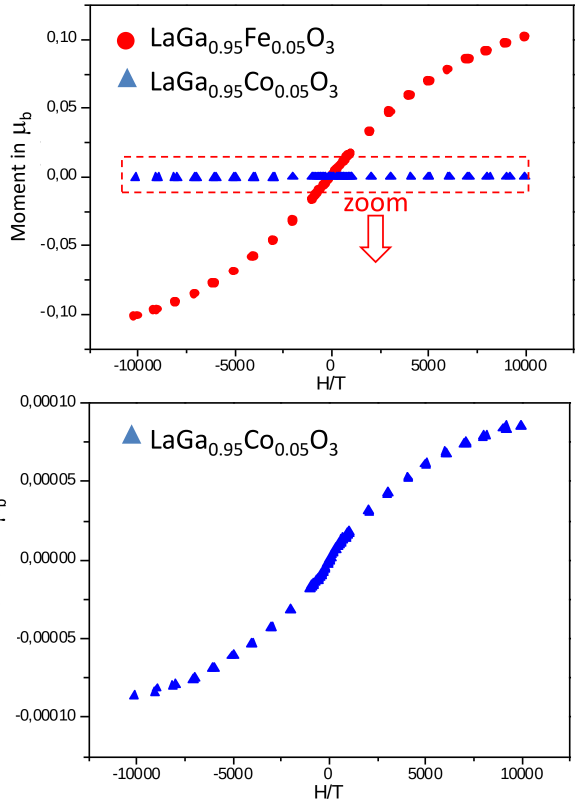

Figure 10: *Top side*- Superimposition of the magnetization curves obtained *versus* H/T ($Oe.K^{-1}$) collected at 5K for 5mol% Co- and Fe-doped $LaGaO_3$ compounds; *Bottom side*- Zoom on the magnetization *versus* H/T of the cobalt compound.

Hence, the main conclusion is that the cobalt is in the LS state, in good agreement with the optical properties characterization and with the previous reported magnetic and optic properties in $LaCo_{0.02}Al_{0.98}Co_{0.02}O_3$.[61] The paramagnetic trend can be simulated in a standard way using a Langevin function. The very low paramagnetic residue, with an intensity about 1/1000 of the signal intensity which was obtained on the Fe-doped compound, can be issued from multiple sources: - paramagnetic impurities (as $Ce^{3+}$ and/or $Tb^{3+}$ and/or $Fe^{3+}$); - occurrence of a negligible fraction of $Co^{2+}$ resulting from minor oxygen content deficiency; - $Co^{3+}$ ions in excited IS or HS state located on crystal surfaces as seen in $LaCoO_3$ nanoparticles;[68] - or from strained ions in the matrix as seen in $LaCoO_3$ thin films.[69]

Seeing the above results on cobalt compounds in the LS state at room temperature, the last part of the study was devoted to the thermal activation of a LS→HS state transition leading to temperature-induced SCO. The study was conducted coupling three *in situ* characterization techniques *versus* temperature: (i) *in situ* optical properties allowing the determination of the evolution of the absorption bands in wavelength and intensities; (ii) *in situ* powder X-ray diffraction to determine the temperature-dependence of the unit cell parameters; (iii) *in situ* magnetic properties allowing the evolution of the magnetization *versus* temperature. The optical and magnetic properties were recorded on the $LaGa_{0.98}Co_{0.02}O_3$ compound for which the color is not too dark, while the structural investigation was made on the $LaGa_{0.9}Co_{0.1}O_3$ composition for which the $Co^{3+}$ ionic radius effects on the unit-cell appear large enough to be determined.

The *in situ* analyses of the optical properties *versus* temperatures under air have brought to the light a drastic modification which can be supposed to be linked to a continuous and broad temperature range LS→HS spin-state modification by increasing the temperatures from room to 600°C, as illustrated Figure 11.

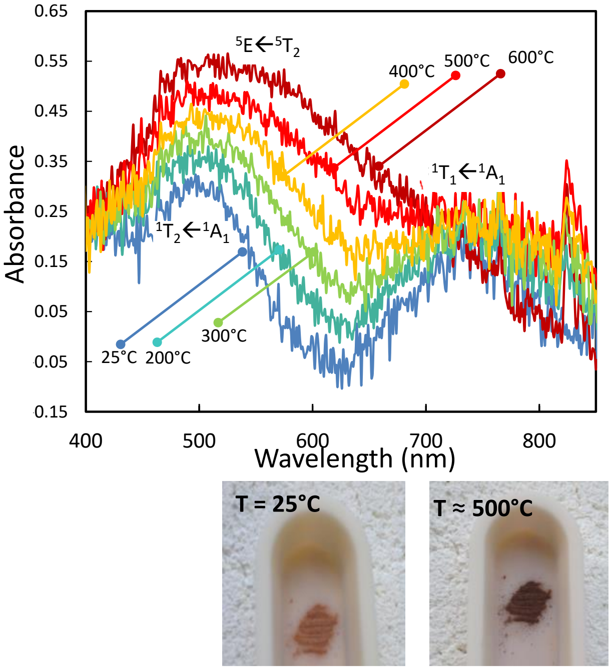

Figure 11: The Co-doped $LaGaO_3$ thermochromic properties showed by *in situ* diffuse reflection recorded between room temperature and 600°C and photographs taken on the as-synthesized sample and a just-quenched sample from 500°C.

The more important change in the absorption spectrum is detected between the applied temperatures 400°C and 500°C. The two room temperature absorption bands disappear progressively to the benefit of a new one located at an intermediate wavelength about 550 nm. From the Tanabe Sugano diagram, the phenomenon is clearly related to the SCO mechanism, the new band at intermediate wavelength could be indexed as the $^5E \leftarrow {}^5T_2$ spin allowed transition. Unfortunately, the phenomenon is not fully achieved at 600°C, but the black body radiation at this temperature starts to mask the electronic transfer absorption and especially, the normalization using black and white reference samples for higher temperature would become quite loose for higher temperatures. In order to try to illustrate the color change associated to the SCO transition, photographs have been taken on the room temperature compound, and a compound just quenched from a high temperature treatment at 600°C (the temperature was estimated very roughly using a thermocouple cabled on the alumina crucible at about 500°C). It can be seen, in agreement with the recorded optical spectra that the color turns form a pale orange-brown at room temperature to a darker brown at about 500°C. After the in situ experiment versus temperature, it can be also noted that the experiment shows the reversibility of the thermochromic phenomenon, the spectrum of the pigment cooled down at room temperature being perfectly superimposed with the starting one.

The ionic radius of $Co^{3+}$ ion in LS and HS configurations significantly differs: Shannon $Co^{3+}$ ionic radius in the LS state is $r_{LS}$=0.545 Å, in the HS state $r_{HS}$ = 0.610 Å. Hence, the SCO should have an impact on the cell parameters. To follow the effect, *in situ* PXRD analyses were performed. Figure 12 shows the $a_R$ and $c_R$ trigonal unit-cell parameters temperature dependence, both expressed as $a_{pc}$ and $c_{pc}$, normalized cell parameters corresponding to the equivalent pseudo-cubic cell: $a_R = a_{pc}\times\sqrt{2}$ and $c_R = c_{pc}\times\sqrt{12}$ for $LaGa_{0.9}Co_{0.1}O_3$ composition. No significant anomaly is highlighted through the spin transition. A roughly linear thermal expansion is indeed observed in the temperature range from room temperature to 700°C. This thermal expansion is about $7\times10^{-6}$ $K^{-1}$ and $12\times10^{-6}$ $K^{-1}$ along the *c* and *a* cell-axis respectively. These values correspond to standard thermal expansion coefficients for $LaGaO_3$ compound,[70] and for iono-covalent cobalt based perovskites.[71] In a relatively sharp manner, at about 700°C, the cell parameters expansion stops and negative thermal expansion for both unit-cell parameters is observed in the range from 700°C to 1000°C. This anomaly in the evolution of the unit-cell parameters would occur in the temperature range corresponding roughly to the end of the SCO but it seems not coherent with the increase of the $Co^{3+}$ ionic radius during the LS→HS spin crossover.

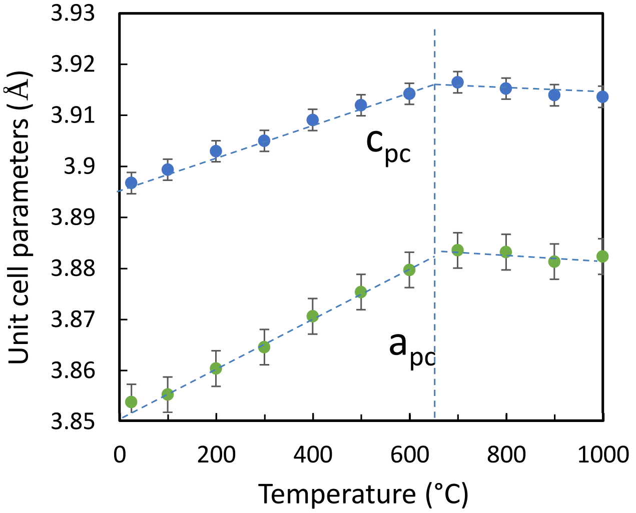

Figure 12: Evolution of the rhombohedral unit-cell parameters extracted from X-ray diffraction patterns *versus* temperature.

At first sight, it should indeed correspond to an increase, and not a decrease, of the unit-cell volume. Furthermore, from the low concentration of cobalt ion, a steric effect of the cobalt ions cannot be the only origin of the anomaly in the evolution of the unit-cell parameters. It can be noted that this very interesting and original observation was also checked on the $LaGa_{0.95}Co_{0.05}O_3$ composition, for which the same behavior is noticed but with a less drastic intensity. The thermal expansion of $LaGaO_3$ with the orthorhombic distortion of perovskite network has already been described and does not show such anomaly[70, 71] in contrast with the unit-cell variation vs temperature of $LaCoO_3$ perovskite. Uhlenbruck et al.[72] and Radaelli et al.[73] described the thermal expansion of $LaCoO_3$ crystallizing with a trigonal symmetry, highlighting spin-state anomalies of the $LaCoO_3$ unit-cell. Both studies show thermal expansion curves becoming steeper with temperature at the beginning of the spin cross over transition and then slightly flatten when the transition is complete but keeping a monotonous behavior. S shape curves for thermal expansion are also known on various Co-based orthorhombic perovskite as in $SmCoO_3$, $NdCoO_3$ or $PrCoO_3$ compounds.[54] That is why this tendency observed for $LaGa_{0.9}Co_{0.1}O_3$ composition better matches the one observed for cobaltite matrix than for gallate perovskite.

Approaches related to the SCO phenomenon can be attempted to explain these observed anomalies. The first approach is to consider that SCO phenomenon should be related to an insulator-metal phase transition with the temperature.[54,70] A metal to insulator phase transition can obviously be related to bond length shortening and so abnormal thermal expansion behavior.[74,75] Sample conductivity measurements *versus* temperature were herein performed until 800°C, but we noticed a pure semi-conductor behavior on the whole temperature range, with the conductivity following a standard Arrhenius plot (see Figure S3). The second approach is to consider that Co-O bond lengths may not be positively correlated to the unit-cell parameters since studied perovskites exhibit steric constrains with too large $Ga^{3+}$ cations besides $La^{3+}$ ionic radius from which a tolerance factor $t < 1$ is calculated. Furthermore, in diluted systems, *i.e.* for small $Co^{3+}$ (LS) cations content diluted in octahedral sub-cationic network formed by larger $Ga^{3+}$ cations, the increase of the Co-O bonds should then decrease some steric strength and surely can be negatively correlated with the unit-cell parameters evolution. It can finally be noted that the anomaly in the evolution of the unit-cell parameters occurs after the SCO phenomenon end rather than during its occurrence. Whatever, the large anomaly recorded on the unit-cell parameters evolution *versus* temperature is without any doubt linked to SCO occurring. This original point is planned to be more deeply investigated in a near future with the help of large facilities: for illustration, temperature dependence X-ray absorption spectroscopy at the O K-edge[74] coupled with neutron powder diffraction study to better describe the rhombohedral phase and especially to determine the rotation angle and strain for the oxygen octahedron with respect to the cobalt content. It can also be noted that counterintuitive decrease of unit-cell parameters during the LS→HS SCO are commonly observed in molecular based materials. In all cases, they are related to significant modifications of the crystal packing often induced by the distortion of the metal coordination sphere.[25,75] Interestingly, this behaviour has been shown by studies performed under pressure to be also associated with Negative Linear Compressibility,[76] and it would certainly be of interest to probe the behaviour of the cobaltites reported herein under pressure.

Finally, a relevant question must be addressed: while the $Co^{3+}$ ion in the HS state has the same ionic radius than $Ga^{3+}$ ($LaGaO_3$) and is also stabilized at room temperature in $LaCoO_3$, why $Co^{3+}$ adopts for low Co content a LS state in $LaGa_{1-x}Co_xO_3$ ? In this case, electronic effects outweigh steric effects. The covalent character of Ga-O chemical bonding with the high electronegativity of $Ga^{3+}$ ($3d^{10}$ : $t_2^6e^4$ , $4s^0$, $\chi_{Pauling} = 1.81$) and the presence of empty 4s orbital contribute to stabilize $t_2^6$ level of LS-$Co^{3+}$ ($t_2^6e0$, $\chi_{Pauling} = 2.01$). At high temperature, the SCO occurs as well as the thermal expansion of 4s and 3d orbitals. Then at T>700°C, we can assume hybridization between 4s(σ*) and $e_g$(σ) orbitals with delocalized electrons as well as strong overlapping between Metal and Oxygen Bands which does not allow the thermal expansion of the M-O chemical bonding.

**Conclusion.**

We have prepared Fe- and Co-doped $La(Al/Ga)O_3$ oxides derived from the cubic perovskite structure. At ambient temperature, the continuous increase of the iron and/or cobalt content into the diamagnetic matrix allows us to tune the chromaticity. Thanks to Mössbauer spectroscopy analysis, the Fe-doped $La(Al/Ga)O_3$ oxides were characterized as paramagnetic species with $Fe^{3+}$ ($3d^5$) in high spin configuration at whatever temperature down to 4K. This is in contrast with the interesting, original and unexpected SCO phenomenon observed on the Co-doped compounds discussed based on *in situ* X-ray diffraction, UV-vis spectroscopy and magnetic measurements up to 750°C. Because of the stabilization of HS-$Co^{3+}$ in $LaCoO_3$ and the ionic size of HS-$Co^{3+}$ close to that of $Ga^{3+}$ ions, the occurrence of $Co^{3+}$ in the LS state in $LaGa_{1-x}Co_xO_3$ solid solution for low Co rate was unexpected. Moreover the higher the Co rate, the higher the crystal field and the SCO phenomenon is then easily observed at lower temperature for lower Co content. Thus, mainly electronic effects and covalence of Ga-O chemical bond are key features to constrain $Co^{3+}$ ions to adopt the LS state in $LaGa_{1-x}Co_xO_3$ solid solutions. This study shows the possibility to use $LaGa_{1-x}Co_xO_3$ compounds as thermal sensor allowing the overcome of the poor cyclability shown by X-chromic oxides and the inadequate low working temperatures shown by molecular complexes.

## AUTHOR INFORMATION

### Corresponding Author

Email: gaudon@icmcb-bordeaux.cnrs.fr

### Author Contributions

The manuscript was written through contributions of all authors. All authors have given approval to the final version of the manuscript.

### Notes

The authors declare no competing financial interests.

## REFERENCES

(1) M.A. Halcrow, *Spin-Crossover Materials: Properties and Applications*, John Wiley & Sons, Ltd., 2013.

(2) S. Hayami, S.M. Holmes, M.A. Halcrow, *J. Mater. Chem. C,* 2015, **3**, 7775-778.

(3) P. Gütlich, A.B. Gaspar, Y. Garcia, *Beilstein J. Org. Chem.*, 2013, **9**, 342-391.

(4) K.S. Murray, H. Oshio, J.A. Real, *Eur. J. Inorg. Chem.*, 2013, **5-6**, 577-580.

(5) O. Kahn, C. Jay Martinez, *Science*, 1998, **279**, 44-48.

(6) J.-F. Létard, P. Guionneau, L. Goux-Capes, *Top. Curr. Chem.*, 2004, **235**, 221-249.

(7) J. Linares, E. Codjovi, Y. Garcia, *Sensors*, 2012, **12**, 4479-4492.

(8) M.D. Manrique-Juárez, S. Rat, L. Salmon, G. Molnár, C.M. Quintero, L. Nicu, H.J. Shepherd, A. Bousseksou, *Coord. Chem. Rev.*, 2016, **308**, 395-408.

(9) M. Cavallini, M. Melucci, *ACS Appl. Mater. Interfaces*, 2015, **7**, 16897-16906.

(10) O. Roubeau, *Chem. Eur. J.*, 2012, **18**, 15230-15244.

(11) G. Aromí, L.A. Barrios, O. Roubeau, P. Gamez, *Coord. Chem. Rev.*, 2011, **255**, 485-546.

(12) L.G. Lavrenova, V.N. Ikorskii, V.A. Varnek, I.M. Oglezneva, S.V. Larionov, *Koord. Khim*., 1986, **12**, 207-215.

(13) Y. Garcia, F. Renz, P. Gütlich, *Curr. Inorg. Chem.*, 2016, **6**, 4-9.

(14) L.G. Lavrenova, O.G. Shakirova, *Eur. J. Inorg. Chem.*, 2013, **5-6**, 670-682.

(15) J.G. Haasnoot, G. Vos, W.L. Groeneveld, *Z. Naturforschung*, 1977, **32b**, 1421-1430.

(16) A. Bousseksou, G. Molnár, L. Salmon, W. Nicolazzi, *Chem. Soc. Rev.*, 2011, **40**, 3313-3335.

(17) M. Gimenez-Marqués, M.L. Garcia-Sanz de Larrea, E. Coronado, *J. Mater. Chem. C.*, 2015, **3**, 7946-7953.

(18) C. Bartual-Murgui, E. Natividad, O. Roubeau, *J. Mater. Chem. C.*, 2015, **3**, 7916-7924.

(19) C. Faulmann, J. Chahine, I. Malfant, D. Caro, B. Cormary, L. Valade, *Dalton Trans.*, 2011, **40**, 2480-2485.

(20) J.M. Herrera, S. Titos-Padilla, S.J.A. Pope, I. Berlanga, F. Zamora, J.J. Delgado, K.V. Kamenev, X. Wang, A. Prescimone, E.K. Brechin, E. Colacio, *J. Mater. Chem.* C., 2015, **3**, 7819-7829.

(21) D. Mader, S. Pillet, C. Carteret, M.J. Stébé, J.L. Blin, *J. Dispers. Sci. Sci. Technol.* **2011**, *32*, 1771-1779.

(22) L. Moulet, N. Daro, C. Etrillard, J.-F. Létard, A. Grosjean, P. Guionneau, *Magnetochemistry*, 2016, **2**, 10-19.

(23) H. Cailleau, M. Lorenc, L. Guérin, M. Servol, E. Collet, M. Buron-Le Cointe, *Acta Crystallogr., Sect. A: Fundam. Crystallogr.*, 2010, **66**, 189-197.

(24) P. Guionneau, E. Collet, *Piezo- and Photo-Crystallography Applied to Spin-Crossover Materials, in Spin-Crossover Materials: Properties and Applications*, ed. M.A. Halcrow, John Wiley & Sons Ltd, Oxford, UK, 2013, Chapter 20, 508-522.

(25) P. Guionneau, *Dalton Trans.*, 2014, **43**, 382-393

(26) M.A. Halcrow, *Chem. Soc. Rev.*, 2011, **40**, 4119-4142.

(27) M. Shatruk, H. Phan, B.A. Chrisostomo, A. Suleimenova, *Coord. Chem. Rev.*, 2015, **289**, 62-73.

(28) S. Alvarez, *J. Am. Chem. Soc.*, 2003, **125**, 6795-6802.

(29) E. König, *Prog. Inorg. Chem.*, 1987, **35**, 527-622.

(30) Y. Iida, Y. Kaneko, Y. Kanno, *J. Mater. Process. Technol.*, 2008, **197**, 261−267.

(31) M. Kovendhan, D.P. Joseph, P. Manimuthu, A. Sendilkumar, S.N. Karthick, S. Sambasivam, K. Vijayarangamuthu, H.J. Kim, B.C. Choi, K. Asokan, C. Venkateswaran, R. Mohan, *Curr. Appl. Physics*, 2015, **15**, 622−631

(32) N. Ozer, C.M. Lampert, *Thin Solid Films*, 1999, **349**, 205−211.

(33) Z. Tong, X. Zhang, H. Lv, N. Li, H. Qu, J. Zhao, Y. Li, X.Y. Liu, *Adv. Mater. Interfaces*, 2015, **2**, 1500230.

(34) Z. Tong, X. Zhang, H. Lv, H. Yang, Y. Tian, N. Li, J. Zhao, Y. Li, *Sci. Rep.*, 2015, **5**, 16864.

(35) Z. Tong, J. Hao, K. Zhang, J. Zhao, B.-L. Su, Y. Li, *J. Mater. Chem. C*, 2014, **2**, 3651−3658.

(36) Y. Wei, J. Zhou, J. Zheng, C. Xu, *Electrochim. Acta*, 2015, **166**, 277−284.

(37) S. Adhikari, D. Sarkar, *RSC Advances*, 2014, **4**, 20145-20153.

(38) R. Ostermann, B. Smarsly, *Nanoscale*, 2009, **1**, 266-270.

(39) P. Delichere, P. Falaras, M. Froment, A. Hugot-Le Goff, B. Agius, *Thin Solid Films*, 1988, **161**, 35-46.

(40) P. Delichere, P. Falaras, A. Hugot-Le Goff, *Thin Solid Films*, 1988, **161,** 47-58.

(41) A.I. Gavrilyuk, *Appl. Surf. Sci.*, 2016, **364**, 498-504.

(42) H. Li, H. Wu, J. Xiao, Y. Su, J. Robichaud, R. Brüning, Y. Djaoued, *Chem. Comm.*, 2016, **52**, 892-895.

(43) C.I. Vargas-Consuelos, K. Seo, M. Camacho-López, O.A. Graeve, *J. Phys. Chem. C*, 2014, **118**, 9531-9537.

(44) A.I. Gavrilyuk, *Appl. Surf. Sci.*, 2013, **273**, 735-747.

(45) T.D. Manning, I.P. Parkin, C. Blackman, U. Qureshi, *J. Mater. Chem.*, 2005, **15**, 4560–4566.

(46) G.A. Niklasson, S.-Y. Li, C.G. Granqvist, *Journal of Physics: Conference Series*, 2014**, 559,** 012001-012007

(47) F. Guinneton, L. Sauques, J.C. Valmalette, F. Cros, J.R. Gavarri, *Thin Solid Films*, 2004, **446**, 287–295.

(48) L.C. Robertson, M. Gaudon, S. Jobic, P. Deniard, A. Demourgues, *Inorg. Chem.*, 2011**, 50**, 2878-2884.

(49) V. Blanco-Gutierrez, A. Demourgues, O. Toulemonde, A. Wattiaux, O. Nguyen, M. Gaudon, *Inorg. Chem.*, 2015, **54**, 2176-2184.

(50) V. Blanco-Gutierrez, A. Demourgues, M. Gaudon, *Dalton Trans.*, 2013, **42**, 13622-13627.

(51) M. Gaudon, C. Carbonera, A.E. Thiry, A. Demourgues, P. Deniard, C. Payen, J.-F. Létard, S. Jobic, *Inorg. Chem.*, 2007, **46**, 10200-10207.

(52) K. Ohta, K. Hirose, K. Shimizu, N. Sata, Y. Ohishi, *Physics of Earth & Planetary Interiors*, 2010, **180**, 154-158.

(53) C. Tassel, H. Kageyama, *Chem. Soc. Rev.*, 2012, **41**, 2025–2035.

(54) K. Knızek, Z. Jirak, J. Hejtmanek, M. Veverka, M. Marysko, G. Maris, T.T.M. Palstra, *Eur. Phys. J. B*, 2005, **47**, 213–220.

(55) M. Korotin, S.Y. Ezhov, I.V. Solovyev, V.I. Anisimov, D.I. Khomskii, G.A. Sawatzky, *Phys. Rev. B*, 1996, **54**, 5309-5316.

(56) G. Maris, Y. Ren, V. Volotchaev, C. Zobel, T. Lorenz, T.T.M. Palstra, *Phys. Rev. B*, 2003**, 67,** 224423.

(57) Asai, K.; Yoneda, A.; Yokokura, O.; Tranquada, J.M.; Shirane, G.; Kohn, K. *J. Phys. Soc. Jpn.*, 1998, **67**, 290-296.

(58) S. Yamaguchi, Y. Okimoto, H. Taniguchi, Y. Tokura, *Phys. Rev. B* 1996, **53**, R2926-R2929.

(59) M.W. Haverkort, Z. Hu, J.C. Cezar, T. Burnus, H. Hartmann, M. Reuther, C. Zobel, T. Lorenz, A. Tanaka, N.B. Brookes, H.H. Hsieh, H.-J. Lin, C.T. Chen, L.H. Tjeng, *Phys. Rev. Lett.*, 2006, **97**, 176405.

(60) V. Křápek, P. Novák, J. Kuneš, D. Novoselov, D.M. Korotin, V.I. Anisimov, *Phys. Rev. B*, 2012, **86**, 195104.

(61) M.N. Sanz-Ortiz, F. Rodrıguez, J. Rodrıguez, G. Demazeau, *J. Phys.: Condens. Matter.*, 2011, **23**, 415501.

(62) Aswin V, A. Dogra, A. Gupta, J.J. Pulikkotil, *RSC Adv.*, 2016, **6**, 1403–1407.

(63) N. Pechini, U.S. Patent No. 3,330,697, 1967.

(64) J. Howard, B.J Kennedy, *J. Phys.: Condens. Matter*, 1999, **11,** 3229–3236.

(65) J. Zhao, N.L. Ross, R.J. Angel, *J. Phys.: Condens. Matter*, 2004, **16**, 8763–8773.

(66) O. Toulemonde, M. Gaudon, *J. Phys. D: Appl. Phys.*, 2010, **43**, 045001-045005.

(67) H. Sérier, O. Toulemonde, D. Bernard, A. Demourgues, J. Majimel, M. Gaudon, *Mater. Res. Bull.*, 2012**, 47**, 755–762.

(68) I. Fita, V. Markovich, D. Mogilyansky, R. Puzniak, A. Wisniewski, L. Titelman, L. Vradman, M. Herskowitz, V.N. Varyukhin, G. Gorodetsky, *Phys. Rev. B*, 2008, **77**, 224421.

(69) D. Fuchs, E. Arac, C. Pinta, S. Schuppler, R. Schneider, H.V. Löhneysen, *Phys. Rev. B*, 2008, **77**, 014434.

(70) W. Marti, P. Fischer, F. Altorfer, H.J. Scheel, M. Tadin, *J. Phys.: Condens. Matter*, 1994, **6,** 127–135.

(71) N. Orlovskaya, M. Lugovy, C. Carpenter, S. Pathak, D. Steinmetz, E. Lara-Curzio, C. Klemenz, M. Radovic, *Acta Materialia*, 2009, **57**, 2984–2992.

(72) S. Uhlenbruck, F. Tietz, *Mater. Sci. Eng. B*, 2004, **107**, 277–282.

(73). P.G. Radaelli, S.-W. Cheong, *Phys. Rev. B* **2002** *66*, 094408

(74) J.L. García-Muñoz, M. Suaaidi, J. Fontcuberta, J. Rodríguez-Carvajal, *Phys. Rev. B*, 1997, **55**, 34-37.

(75) J.K. Burdett, S.A. Gramsch, L. Smith, *Z. anorg. allg. Chem.*, 1996, **622**, 1667-1676.

(76) O. Toulemonde, N. N'Guyen, F. Studer, A. Traverse, *J. Solid State Chem.*, 2001, **158**, 208-217.

(77) S. Lakhloufi, M.H. Lemée-Cailleau, G. Chastanet, P. Rosa, N. Daro, P. Guionneau, *Phys. Chem. Chem. Phys.*, 2016, **18**, 28307-28315.

(78) H.J. Shepherd, T. Palamarciuc, P. Rosa, P. Guionneau, G. Molnár, J.-F. Létard, A. Bousseksou, *Angew. Chem. Int. Ed.*, 2012, **51**, 3910-3914.

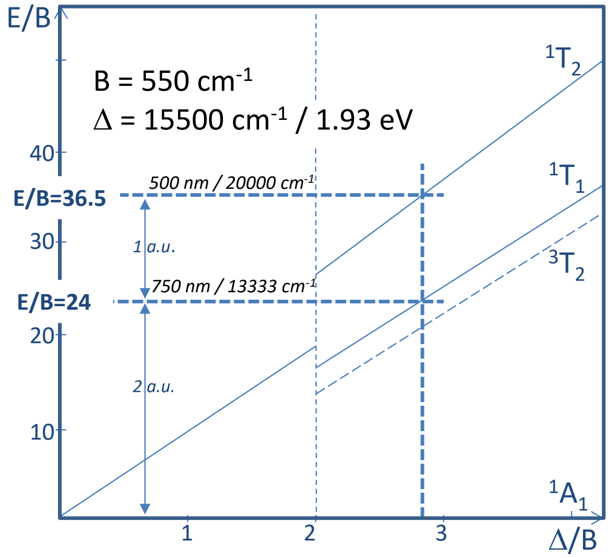

Figure S1: Extraction method of Racah parameter B and crystal field Δ for an attribution of 1st allowed and 2nd allowed transition equal respectively to 750 nm and 500 nm.

The way we have extracted the Racah parameter B and the crystal field is based on a trivial graphic exploitation of the Tanabe-Sugano diagram for *d7* configuration. The above Figure shows that the shoulder of absorbance observed at about 850 nm could correspond to the forbidden transition from $^1A_1$ to $^3T_2$ state.

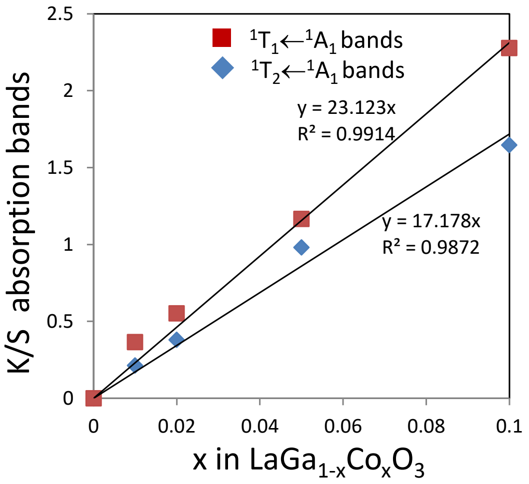

Figure S2: Kubelka-Munk transform ($K/S = (1 - R^2)/(2R)$ with $1-R = A$, R: Reflectivity, A: Absorption) of the two absorption bands (after background subtraction) associated with the d-d $Co^{3+}$ ion transitions.

The nearly linear relation between K/S intensities and the doping ion concentration shows non-deviation between the cobalt target concentration and the efficient concentration inside the perovskite material.

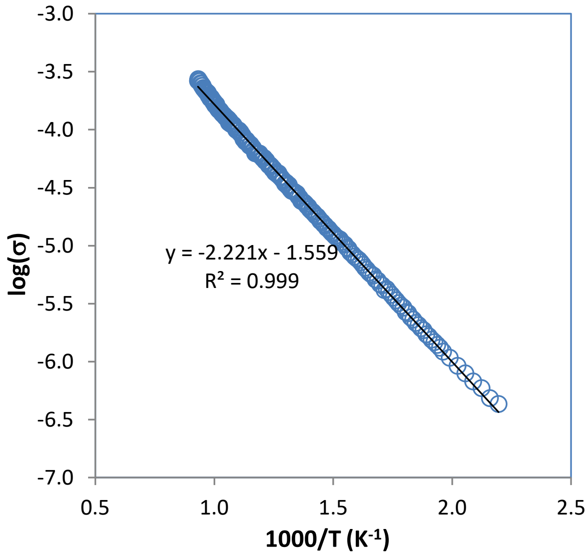

Figure S3: Arrhenius-type plot of the conductance. Data are represented by the open circles and the line is a fit of the raw data considering an activation energy model for the conductance.

Resistivity measurement was carried out using a standard home made four-probe dc technique

For Table Of Content only

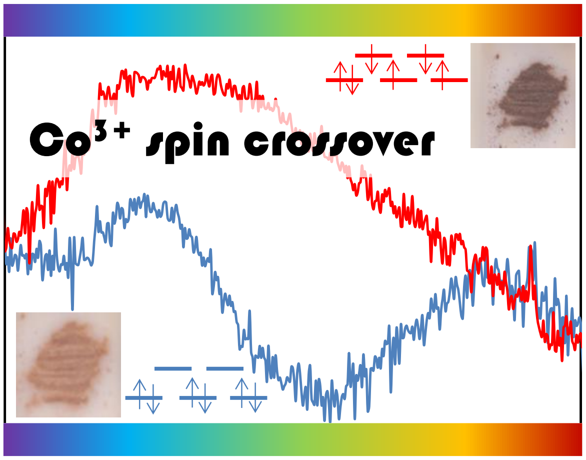

## Synopsis

Thanks to spin-crossover phenomenon, Co-doped La(Al/Ga)$O_3$ compounds with perovskite structure are shown to be usefull as thermal sensor allowing the overcome of the poor cyclability shown by X-chromic oxides and the inadequate low working temperatures shown by molecular complexes.